Essential title page information

Title.

CTSSP: A Temporal-Spectral-Spatial Joint Optimization Algorithm for Motor Imagery EEG Decoding

Author names and affiliations.

Lincong Pan [a,b], panlincong@tju.edu.cn
Kun Wang [a,c] , flora_wk@tju.edu.cn
Weibo Yi [d] , yiweibo1987@163.com
Yang Zhang [e], zhangyang982003@163.com
Minpeng Xu [a,c] , minpeng.xu@tju.edu.cn
Dong Ming [a,c] , richardming@tju.edu.cn

[a] Academy of Medical Engineering and Translational Medicine, Tianjin University, Tianjin 300072, People's Republic of China
[b] School of Precision Instruments and Optoelectronics Engineering, Tianjin University, Tianjin 300072, People's Republic of China
[c] Haihe Laboratory of Brain-computer Interaction and Human-machine Integration, Tianjin 300392, People's Republic of China
[d] Beijing Machine and Equipment Institute, Beijing 100192, People's Republic of China
[e] Rehabilitation and Physical Therapy Department, Shandong University of Traditional Chinese Medicine Affiliated Hospital, Jinan 250011, People's Republic of China

* ***Corresponding author.***

flora_wk@tju.edu.cn (K. Wang)
minpeng.xu@tju.edu.cn (M. Xu)

Abstract

Objective: Motor imagery brain-computer interfaces (MI-BCIs) are crucial for neuro-rehabilitation and assistive therapy, but decoding motor imagery electroencephalography (EEG) signals is challenged by non-stationarity, low signal-to-noise ratio, and cross-session variability. ***Methods***: We propose the common temporal-spectral-spatial patterns (CTSSP) algorithm to address these challenges. The method introduces: (1) a multi-time-window design to capture dynamic neural patterns, (2) an adaptive finite impulse response (FIR) filter bank to suppress noise and amplify task-relevant features across time windows and channels, and (3) a regularization constraint to improve robustness and prevent overfitting. ***Results***: CTSSP outperforms existing methods, achieving an average classification accuracy of 76.9% for within-subject and 68.8% for cross-session tasks across five publicly available datasets. In within-subject scenarios, it surpasses competing methods by 2.6% to 14.6% ($p < 0.001$), while in cross-session scenarios, it outperforms others by 2.4% to 13.8% ($p < 0.05$). Visualized filters confirm the alignment with motor cortex neural mechanisms. ***Conclusion***: CTSSP provides an effective solution to extract dynamic temporal-spectral-spatial features, improving classification accuracy in MI-BCI tasks. ***Significance***: The CTSSP algorithm offers a robust, interpretable method for MI-BCI systems, enhancing performance in noisy, non-stationary environments and advancing neuro-rehabilitation applications. The code for this research is available at https://github.com/PLC-TJU/CTSSP.

Keywords: Electroencephalography (EEG), Brain-computer interface (BCI), Motor imagery (MI), temporal-spectral-spatial joint optimization, cross-session decoding

1. Introduction

Brain-computer interface (BCI) establishes a direct communication pathway between neural activity and external devices by decoding brain signals into executable commands, bypassing traditional neuromuscular pathways[1]. Among the various BCI applications, motor imagery BCI (MI-BCI) has emerged as a prominent research area, as it identifies specific neural patterns associated with users imagining bodily movements[2]. Unlike BCI systems that rely on actual physical movements, MI-BCI can activate motor-related brain regions without requiring physical actions, offering significant potential in areas such as neural rehabilitation and assistive therapy[3,4]. For instance, in patients with stroke or spinal cord injuries, MI-BCI can facilitate motor function reorganization through real-time feedback, thereby accelerating the rehabilitation process[5–7]. A major challenge in MI-BCI technology lies in extracting task-related neural features from complex, weak, and non-stationary EEG signals to achieve high-precision classification[8].

Electroencephalography (EEG), with its millisecond temporal resolution, non-invasive nature, and low cost, has become the primary signal modality in MI-BCI research[4,9]. Motor imagery tasks induce rhythmic activity changes in specific frequency bands within the brain's motor cortex. Energy suppression, or event-related

desynchronization (ERD), typically occurs in the alpha band (8–13 Hz) and beta band (14–30 Hz), which are associated with the early stages of motor preparation[10]. In contrast, energy enhancement, or event-related synchronization (ERS), appears in the later stages of motor execution[11]. Moreover, different motor imagery tasks (e.g., left hand, right hand, or foot movement) activate distinct areas of the contralateral motor cortex, producing recognizable spatial patterns. For instance, right-hand imagery primarily activates the left central region (near electrode C3), while foot imagery is more concentrated in the midline area (near electrode Cz)[12]. The dynamic coupling of these temporal, spectral, and spatial features underpins the theoretical basis for MI-EEG decoding, though it also imposes higher demands on the algorithm's capacity to jointly model multiple domains [13].

However, the inherent non-stationarity, low signal-to-noise ratio (SNR), and cross-session variability of MI-EEG signals significantly limit the performance of traditional methods[13]. Non-stationarity refers to the temporal changes in signal statistical properties, such as shifts in ERD and ERS due to factors like fatigue or attention fluctuations[14]. Low SNR results from interference from electromyography (EMG), electrooculography (EOG), and weak cortical neural activity (< 10 μV)[15]. Moreover, in cross-session scenarios, factors such as electrode impedance changes and head movement further exacerbate signal variability, leading to a considerable decline in the generalization ability of existing algorithms[16,17]. For example, the classic common spatial patterns (CSP) algorithm optimizes spatial filters to maximize the variance difference between two signal classes[12], but its performance may decrease by more than 10% in cross-session experiments[13].

To address these challenges, several improvement strategies have been proposed[8]. Early methods focused on single-domain optimization of temporal, spatial, or spectral features[18–23]. The common spatial spectral pattern (CSSP) method significantly enhanced single-trial EEG classification performance by jointly designing spatial projection matrices and finite impulse response (FIR) filters[18]. However, its fixed time window assumption limits its adaptability to the non-stationarity of the signals. The filter bank CSP (FBCSP) approach decomposes EEG signals into multiple sub-frequency bands to improve discriminability, but its performance heavily depends on manually predefined frequency bands and overlooks the dynamic coupling characteristics in the time domain[24]. To address these limitations, the temporally constrained sparse group spatial patterns (TSGSP) algorithm introduced temporal smoothing constraints and joint sparse optimization to extract CSP features from multiple time windows and frequency bands[25]. However, it still relies on manually predefined time windows and frequency bands, and its high computational complexity hinders its suitability for real-time BCI systems, which require low latency.

In recent years, deep learning techniques have provided data-driven solutions for MI-EEG decoding[26–28]. Convolutional neural networks (CNNs) address the limitations of manual feature design by enabling end-to-end learning of temporal and spatial features[29]. For instance, ShallowConvNet (sCNN) mimics the frequency band power feature extraction process of FBCSP using a shallow architecture, while

DeepConvNet (dCNN) captures multi-scale abstract features through a deep residual structure[30]. EEGNet improves model efficiency by employing depthwise separable convolutions to reduce the parameter count[31], although its sensitivity to electrode shifts in cross-session scenarios limits its clinical applicability[13]. The lightweight multi-dimensional attention network (LMDA-Net) enhances feature selectivity through channel-time-space attention mechanisms[32], while Tensor-CSPNet integrates Riemannian manifold optimization with tensor decomposition to improve spatial discriminability within a geometric deep learning framework[33,34].

Recently, SBLEST (Sparse Bayesian Learning for End-to-End EEG Decoding) achieved joint optimization of spectral and spatial features through Bayesian modeling[35]. Its core advantages include: (1) Adaptive sparsity, which automatically selects task-related spectral and spatial features without requiring preset regularization parameters; and (2) Multi-domain joint modeling, which simultaneously optimizes spatial projections and spectral weights within a unified probabilistic framework. Experiments demonstrate that SBLEST significantly outperforms traditional machine learning and deep learning algorithms, such as CSP and EEGNet, in both within-subject and cross-subject MI-EEG classification tasks[35]. However, SBLEST fails to account for the non-stationarity and cross-session variability of MI-EEG signals and lacks adaptive modeling of temporal dynamics. Additionally, there has been no performance evaluation of SBLEST in MI-EEG cross-session classification tasks.

Despite the progress made by these methods, a common limitation persists in the disconnected modeling of temporal, spectral, and spatial features. Traditional methods rely on manually set parameters, while deep learning models, despite their ability to automatically extract features, often lack explicit modeling of neurophysiological mechanisms, leading to insufficient interpretability and limited cross-domain generalization. To address these challenges, this paper proposes the common temporal-spectral-spatial patterns (CTSSP) algorithm. The core innovation of CTSSP lies in constructing a unified optimization framework that simultaneously learns joint filters across the temporal, spectral, and spatial domains:

1) Temporal Adaptability: Captures the dynamic evolution of neural responses (e.g., the transition from ERD to ERS) through multiple time windows.
2) Frequency Adaptability: Enhances the representation of temporal features by incorporating delay-augmented techniques and flexibly constructing FIR filters for different channels, thereby dynamically suppressing noise and enhancing task-relevant rhythms.
3) Spatial Discriminability: Optimizes spatial weights to focus on task-relevant brain areas in the motor cortex.

The remainder of this paper is organized as follows: Section 2 provides the mathematical formulation of the CTSSP algorithm. Section 3 details the experimental setup, including descriptions of the five public datasets, data preprocessing methods, nine competing algorithms, experimental designs for both within-subject and cross-session classification tasks, and the statistical analysis techniques employed. Section 4 discusses the key features of CTSSP, its limitations, and potential directions for future

work. Finally, Section 5 presents the conclusion of the paper. For ease of reference, **Table 1** lists the key mathematical symbols used throughout the paper.

Table 1. List of symbols used in this paper

N_c: number of channels
N_t: number of sampled time points
N_d: order of the optimized FIR filters
N_t: number of selected time windows
k: number of selected filters
$\mathbf{X} \in \mathbb{R}^{\mathrm{N}_c \times \mathrm{N}_t}$: data matrix of single-trial EEG data
$\mathbf{X}_{(d)} \in \mathbb{R}^{\mathrm{N}_c \times \mathrm{N}_t}$: data matrix with a delay of d time steps applied to $\mathbf{X}$
$\widetilde{\mathbf{X}} \in \mathbb{R}^{\mathrm{N}_d\mathrm{N}_c \times \mathrm{N}_t}$: time-delayed augmented data matrix
$\mathbf{C}_t^{(1)}, \mathbf{C}_t^{(2)} \in \mathbb{R}^{\mathrm{N}_d\mathrm{N}_c \times \mathrm{N}_d\mathrm{N}_c}$: mean covariance matrices of $\widetilde{\mathbf{X}}$ under two states from the t-th time window
$\tilde{\mathbf{C}}^{(1)}, \tilde{\mathbf{C}}^{(2)} \in \mathbb{R}^{\mathrm{N}_t\mathrm{N}_d\mathrm{N}_c \times \mathrm{N}_t\mathrm{N}_d\mathrm{N}_c}$: mean block-diagonally augmented covariance matrices under two states
$\mathbf{s} \in \mathbb{R}^{\mathrm{N}_c \times 1}$: spatial filter
$\mathrm{s}_c \in \mathbb{R}^1$: spatial filter weight for the c-th channel
$\mathbf{a}_c \in \mathbb{R}^{\mathrm{N}_d \times 1}$: FIR filter for the c-th channel
$\mathbf{A} \in \mathbb{R}^{\mathrm{N}_d \times \mathrm{N}_c}$: FIR filter for all channels
$\mathbf{u} \in \mathbb{R}^{\mathrm{N}_d\mathrm{N}_c \times 1}$: combined spectral-spatio filter
$\mathbf{u}_t \in \mathbb{R}^{\mathrm{N}_d\mathrm{N}_c \times 1}$: combined temporal-spectral-spatial filter for the t-th time window
$\mathbf{u}_{tc} \in \mathbb{R}^{\mathrm{N}_d \times 1}$: combined temporal-spectral-spatio filter for the t-th time window and the c-th channel
$\mathbf{w} \in \mathbb{R}^{\mathrm{N}_t\mathrm{N}_d\mathrm{N}_c \times 1}$: combined temporal-spectral-spatial filter in a single dimension
$\mathbf{W} \in \mathbb{R}^{\mathrm{N}_t\mathrm{N}_d\mathrm{N}_c \times \mathrm{N}_t\mathrm{N}_d\mathrm{N}_c}$: estimated low-rank weight matrix

2. Method

The CTSSP algorithm assumes that MI-EEG signals exhibit distinct frequency responses and spatial topological patterns at different time intervals, a hypothesis supported by neurophysiological evidence[10,11]. The core objective of this method is to jointly optimize temporal, spectral, and spatial filters to maximize the variance (energy) difference between the two signal classes after filtering.

The objective function of CTSSP is derived from augmented data, which includes both the original EEG signals and their delayed copies from multiple time windows. To begin, we first consider the case of a single filter. Let $\mathbf{X} \in \mathbb{R}^{\mathrm{N}_c \times \mathrm{N}_t}$ represent an EEG sample, and $\mathbf{s} = [\mathrm{s}_1, \mathrm{s}_2, \dots, \mathrm{s}_{\mathrm{N}_c}]^{\mathrm{T}} \in \mathbb{R}^{\mathrm{N}_c \times 1}$ denote the spatial filter vector. The spatial filtering process can be expressed as:

$$\mathbf{X}_{\mathrm{spatial}} = \sum_{c=1}^{\mathrm{N}_c} \mathrm{s}_c \mathbf{X}(c, :) \tag{1}$$

where $\mathbf{X}(c,:)$ represents the c-th row of the original data matrix $\mathbf{X}$, i.e., the EEG signal from the c-th channel.

Furthermore, let $\mathbf{a}_c \in \mathbb{R}^{\mathrm{N}_d \times 1}$ denote the FIR filter vector for the c-th channel. The spectral filtering process can be formulated as follows:

$$\mathbf{X}_{\mathrm{freq}}(c,n) = \sum_{d=0}^{N_d-1} \mathbf{a}_c\,(d) \cdot \mathbf{X}(c,n-d) \tag{2}$$

where $\mathbf{X}_{\mathrm{freq}}(c,n)$ represents the signal value of the c-th channel at the n-th time point after spectral filtering.

By combining spatial and spectral filtering, the overall filtering process can be formalized as:

$$\mathbf{z} = \mathbf{u}^{\mathrm{T}}\widetilde{\mathbf{X}} \tag{3}$$

where $\mathbf{A} = [\mathbf{a}_1, \mathbf{a}_2, \dots, \mathbf{a}_{\mathrm{N}_c}] \in \mathbb{R}^{\mathrm{N}_d \times \mathrm{N}_c}$ represents the matrix of FIR filter vectors for all channels, and $\mathbf{u} = \mathrm{vec}((\mathbf{s}^{\mathrm{T}} \odot \mathbf{A})^{\mathrm{T}})$ denotes the re-parameterized spectral-spatial filter vector, expressed as:

$$\mathbf{u} = \left[\mathrm{s}_1{\mathbf{a}_1}^{\mathrm{T}}, \mathrm{s}_2{\mathbf{a}_2}^{\mathrm{T}}, \dots, \mathrm{s}_{\mathrm{N}_c}{\mathbf{a}_{\mathrm{N}_c}}^{\mathrm{T}}\right]^{\mathrm{T}} \in \mathbb{R}^{\mathrm{N}_d\mathrm{N}_c \times 1} \tag{4}$$

Additionally, $\widetilde{\mathbf{X}} \in \mathbb{R}^{\mathrm{N}_d\mathrm{N}_c \times \mathrm{N}_t}$ represents the augmented data matrix, constructed by delayed copies of the original signal $\mathbf{X}$, with the following structure:

$$\widetilde{\mathbf{X}} = \begin{bmatrix} \mathbf{X}_{(0)} \\ \mathbf{X}_{(1)} \\ \vdots \\ \mathbf{X}_{(N_d-1)} \end{bmatrix} \tag{5}$$

where $\mathbf{X}_{(d)}$ represents the version of $\mathbf{X}$ delayed by d time points, with $d \in \{0,1,\dots,N_d-1\}$.

Based on this, we define the objective function of CTSSP, which aims to maximize the variance difference between the two signal classes by jointly optimizing spectral-spatial filters across different time windows. The objective function can be intuitively expressed as:

$$\begin{aligned} \mathcal{J}(\mathbf{u}_1, \mathbf{u}_2, \dots, \mathbf{u}_{\mathrm{N_t}}) &= \max_{\mathbf{u}_1,\mathbf{u}_2,\dots,\mathbf{u}_{\mathrm{N_t}}} \sum_{t=1}^{\mathrm{N_t}} \mathbf{u}_t^{\mathrm{T}} \mathbf{C}_t^{(1)}\, \mathbf{u}_t \\ s.t. \sum_{t=1}^{\mathrm{N_t}} \mathbf{u}_t^{\mathrm{T}} \mathbf{C}_t^{(2)}\, \mathbf{u}_t &= 1 \end{aligned} \tag{6}$$

where $\mathbf{u}_t$ represents the spectral-spatial filter vector for the t-th time window, and $\mathbf{C}_t^{(1)}$ and $\mathbf{C}_t^{(2)}$ are the covariance matrices of the augmented data matrix $\widetilde{\mathbf{X}}$ for the two classes, computed for the t-th time window, with $t \in \{1,2,\dots,\mathrm{N}_t\}$.

We introduce $\mathbf{w}$ as the new global filter vector, and the above objective function can be simplified into a generalized Rayleigh quotient form:

$$\mathcal{J}(\mathbf{w}) = \max_{\mathbf{w}} \mathbf{w}^{\mathrm{T}} \tilde{\mathbf{C}}^{(1)} \mathbf{w}$$

$$s.t.\,\mathbf{w}^{\mathrm{T}}\tilde{\mathbf{C}}^{(2)}\mathbf{w}=1 \tag{7}$$

where:

$$\tilde{\mathbf{C}}^{(1)}=\begin{bmatrix} C_1^{(1)} & \cdots & \mathbf{0} \\ \vdots & \ddots & \vdots \\ \mathbf{0} & \cdots & C_{\mathrm{N_t}}^{(1)} \end{bmatrix}, \tilde{\mathbf{C}}^{(2)}=\begin{bmatrix} C_1^{(2)} & \cdots & \mathbf{0} \\ \vdots & \ddots & \vdots \\ \mathbf{0} & \cdots & C_{\mathrm{N_t}}^{(2)} \end{bmatrix}, \mathbf{w}=\begin{bmatrix} \boldsymbol{u}_1 \\ \boldsymbol{u}_2 \\ \vdots \\ \boldsymbol{u}_{N_t} \end{bmatrix} \tag{8}$$

Using Lagrange multipliers, we can easily derive the following:

$$\tilde{\mathbf{C}}^{(1)}\mathbf{w}=\lambda\tilde{\mathbf{C}}^{(2)}\mathbf{w} \tag{9}$$

where the solution for the filter vector $\mathbf{w}\in\mathbb{R}^{\mathrm{N}_t\mathrm{N}_d\mathrm{N}_c\times 1}$ can be obtained through generalized eigenvalue decomposition.

For the calculation of multiple filters and to avoid overfitting, we further improve the objective function in equation (7) by introducing a penalty term to constrain the number of potential filters:

$$\mathcal{J}(\mathbf{W})=\min_{\mathbf{W}}\mathrm{tr}\left(\mathbf{W}^{\mathrm{T}}\tilde{\mathbf{C}}^{(1)}\mathbf{W}\right)+\rho\cdot\mathrm{rank}(\mathbf{W})$$

$$s.t.\,\mathbf{W}^{\mathbf{T}}\tilde{\mathbf{C}}^{(2)}\mathbf{W}=\mathbf{I} \tag{10}$$

where $\mathbf{W}\in\mathbb{R}^{\mathrm{N}_t\mathrm{N}_d\mathrm{N}_c\times\mathrm{N}_t\mathrm{N}_d\mathrm{N}_c}$ represents the low-rank filter matrix, $\mathrm{tr}(\cdot)$ denotes the trace of a matrix, $\mathrm{rank}(\cdot)$ denotes the rank of a matrix, and ρ is the regularization parameter.

We solve equation (10) using sparse Bayesian learning (SBL)[35], which automatically determines the regularization parameters and the number of filters. This eliminates the need for cross-validation, enabling more efficient use of the data and reducing computational costs. Finally, for each new test sample $\tilde{\mathbf{C}}_{\mathrm{test}}$, its classification result is given by:

$$\hat{\mathbf{y}}_{\mathrm{test}}=\mathrm{sign}\left(\mathrm{tr}\left(\mathbf{W}^{\mathrm{T}}\tilde{\mathbf{C}}_{\mathrm{test}}\right)\right) \tag{11}$$

where $\mathrm{sign}(\cdot)$ is the sign function. Once $\mathbf{W}$ is determined, the spectral-spatial filter $\mathbf{u}_t$ for each time window can be decomposed into the spatial filter $\mathbf{s}$ and the corresponding spectral filters $\mathbf{a}_c$[36], as follows:

$$\mathrm{s}_c=\mathrm{sign}\left(\mathbf{u}_{tc}(1)\right)\cdot\|\mathbf{u}_{tc}\|_2 \tag{12}$$

$$\mathbf{a}_c=\mathbf{u}_{tc}/\mathrm{s}_c \tag{13}$$

where $\mathbf{u}_{tc}=\mathrm{s}_c\mathbf{a}_c{}^{\mathrm{T}}=\mathbf{u}_t(\mathrm{N}_d(c-1)+1,\ldots,\mathrm{N}_d c)$ is the weight coefficient for the signal and its delayed version in the c-th channel at the t-th time window.

3. Experiments

3.1 Datasets

The proposed CTSSP algorithm was evaluated on five publicly available datasets and compared with nine other advanced methods based on classification accuracy. These datasets include BNCI2014001[37], Lee2019[38], Pan2023[13], BNCI2014002[39], and Cho2017[40]. Among these, the first three datasets include data from two sessions per subject, while the last two datasets contain data from only one session per subject. Each dataset consists of two class labels: left/right-hand MI or right-hand/foot MI,

with an equal number of samples for each class. All datasets are accessible online through the MOABB software package[41]. **Table 2** provides detailed information about these datasets.

Table 2. Details of all datasets

Dataset	Name	Classes	Sessions	Trials	Channels	Duration(s)	Subjects
Dataset I	BNCI2014001	left/right hand	2	288	22	4	9
Dataset II	Lee2019	left/right hand	2	200	62	4	54
Dataset III	Pan2023	left/right hand	2	240	28	4	14
Dataset IV	BNCI2014002	right hand/feet	1	160	15	5	14
Dataset V	Cho2017	left/right hand	1	200	64	3	52
Total:							143

3.2 Preprocessing

We applied a fourth-order Butterworth bandpass filter with a frequency range of 8–32 Hz to all datasets. For datasets II and V, we used only the recommended 20 signal channels (FC-5/3/1/2/4/6, C-5/3/1/z/2/4/6, and CP-5/3/1/z/2/4/6)[38]. For dataset IV, we retained only the first 4 seconds of each sample. To ensure consistency in EEG signal distributions, we applied Euclidean alignment[42] and whitening to both the training and testing data. Importantly, we used the same whitening matrix derived from the training set for the test set to avoid data leakage.

3.3 Classification Methods

Fig. 1 illustrates the data processing pipeline of the CTSSP algorithm. To evaluate the effectiveness of CTSSP, we compared it with nine representative or advanced methods as follows:

1) **CSP**: Spatial filtering with CSP[12], followed by extraction of the most discriminative k features, and classification using Linear Discriminant Analysis (LDA).
2) **CSSP**: Spatial-spectral filtering using CSSP[18], with FIR filter order $\mathrm{N}_d = 2$ and time delays $d \in \{0,1\}$, followed by extraction of the most discriminative k features and classification with LDA.
3) **FBCSP**: A filter bank with six sub-bands: 8–12 Hz, 12–16 Hz, 16–20 Hz, 20–24 Hz, 24–28 Hz, and 28–32 Hz. CSP is used to extract the most discriminative k features from each sub-band, followed by mutual information-based feature selection to retain the top 10 discriminative features[24], and classification with LDA.
4) **SBLEST**: Spectral-spatial filtering and classification using SBLEST[35], with FIR filter order $\mathrm{N}_d = 2$ and time delays $d \in \{0,1\}$.
5) **sCNN:** Classification with ShallowConvNet[30], a shallow convolutional neural network designed for EEG signal classification, consisting of time and space convolution layers with 40 filters each, along with pooling and dropout layers (dropout rate of 0.5) to enhance feature extraction and prevent overfitting.
6) **dCNN:** Classification with DeepConvNet[30], a deep convolutional neural network model with multiple convolutional and pooling layers for hierarchical

feature extraction. The first layer contains 25 temporal-spatial filters, followed by 3 convolution-max-pooling layers and dropout layers (dropout rate of 0.5).

7) **EEGNet:** Classification with EEGNet[31], a compact convolutional neural network designed for EEG signal processing. It uses depthwise and separable convolutions to capture spatial and temporal features, with a structure consisting of an initial layer with 8 time filters and a depthwise convolution layer with 16 space filters, with a dropout rate of 0.25.
8) **LMDA-Net:** Classification with LMDA-Net[32], which consists of a baseline network, a channel attention module, and a deep attention module. The channel attention module introduces spatial information filtering through tensor products, while the deep attention module enhances cross-temporal-spatial feature integration using the Hadamard product. LMDA-Net uses 24 time filters and 9 space filters.
9) **CSPNet:** Classification with Tensor-CSPNet[34], which includes three modules: the SPD manifold encoding module that encodes sample covariance matrices as tensor representations, the feature extraction module using 3D convolution networks to extract relevant temporal-spectral-spatial features, and the classification module performing MI-EEG classification. The Tensor-CSPNet in this paper applies the same 6 sub-bands as FBCSP and 3 or 4 sub-time windows (for dataset V: 0–1s, 1–2s, 2–3s; for other datasets: 0–1s, 1–2s, 2–3s, 3–4s).

For CSP, CSSP, and FBCSP, the optimal feature dimension k is determined by cross-validation on the training set, with the search range [2,4,6,8,10,12,14,16,18,20]. CTSSP uses the same FIR filter order $\mathrm{N}_d = 2$ and delay points $d \in \{0,1\}$ as CSSP and SBLEST, and the number of time windows $\mathrm{N}_t = 3$ (for dataset V: 0–2s, 0.5–2.5s, 1–3s; for other datasets: 0–3s, 0.5–3.5s, 1–4s). All deep learning methods employ the Adam optimizer with an initial learning rate of 0.001, dynamically adjusted by the *CosineAnnealingLR* scheduler. We trained the neural network models for up to 300 epochs, with early stopping if the loss did not change significantly within 50 consecutive epochs.

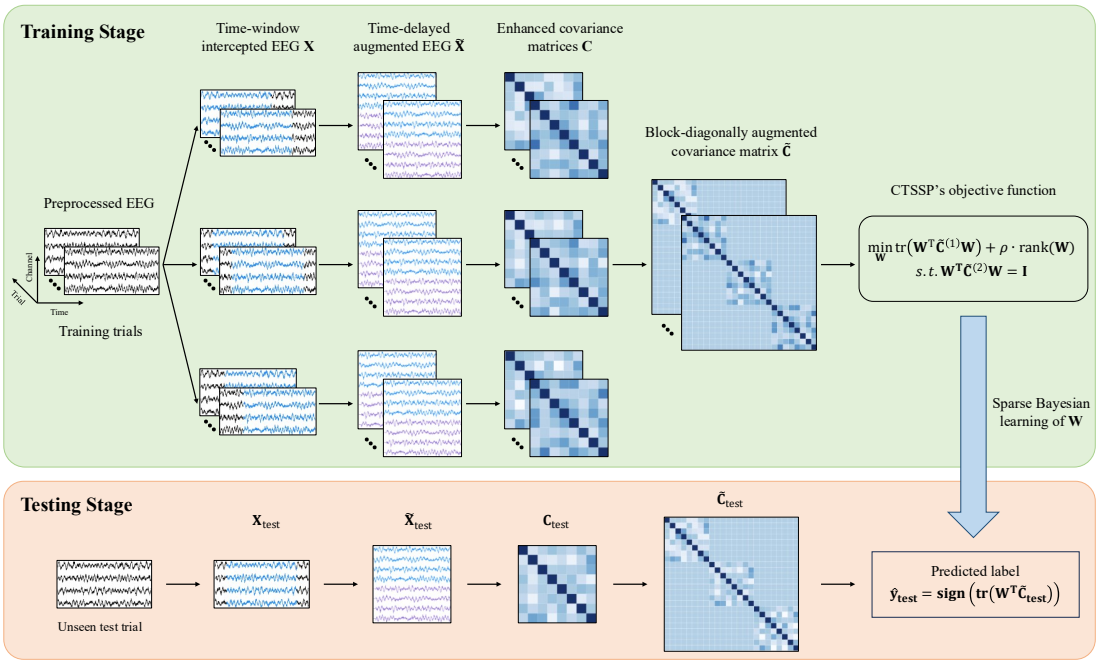

Fig.1. Data processing pipeline of the CTSSP algorithm

3.4 Experimental Design

We evaluate the methods in two scenarios:

1) Within-subject classification experiment: We performed this experiment on all five publicly available datasets. For the first three datasets, we randomly mixed the samples from two sessions of each subject. We trained the classification models of different algorithms on the training set and tested them on the same subject's test set. We divided the training and test sets using 10-fold stratified cross-validation, repeated 5 times. The average of the 50 classification results was used as the final classification outcome. This experiment aimed to evaluate the classification performance of different methods within the same subject.
2) Cross-session classification experiment: We performed this experiment on the first three publicly available datasets. We used all the samples from the first session of each subject as the training set and all the samples from the second session as the test set. This experiment aimed to simulate real-world application scenarios and evaluate the classification performance of different methods in a fully cross-session scenario.

3.5 Statistical Analysis

We performed statistical analysis using the methods described in [41]. Specifically, we analyzed the balanced accuracy of different algorithms for each subject and conducted the following statistical tests: For datasets with fewer than 20 subjects, we used a permutation-based t-test to assess differences between two algorithms. For datasets with 20 or more subjects, we applied the Wilcoxon signed-rank test for comparison. These tests aimed to calculate the p-value for the null hypothesis that "one algorithm is not superior to the other." To aggregate results across different datasets, we used the Stouffer method for meta-analysis of the p-values from each

dataset. The Stouffer method involves converting each *p*-value into a standard normal score, summing these scores, and calculating the overall *p*-value for each algorithm pair based on the summed result. This approach integrates multiple independent tests, providing more reliable statistical conclusions.

4. Results

4.1 Visualization of Filters

Fig. 2 presents the scalp topographies of the spatial filters and the corresponding amplitude-frequency response curves for the three primary channels (C3, Cz, and C4) of a typical subject (S5) from dataset I, using various algorithms. Additional visual results for other datasets and subjects are provided in **Appendix A**. For CTSSP, the spatial and spectral filter coefficients for each time window are computed as described in **Eqs. (12)** and **(13)**. Since the CSP algorithm does not incorporate temporal-spectral filtering, its amplitude-frequency response curve remains constant at 1. The weight maps and amplitude-frequency response curves for CSP, CSSP, and SBLEST are linked to the most discriminative eigenvalues, whereas those for CTSSP are derived from the most discriminative eigenvalues across three time windows. The results show that the scalp topography generated by CTSSP primarily focuses on task-relevant regions of the motor cortex. Furthermore, the spatial filter weight distribution and temporal-spectral response for each time window exhibit significant variations, supporting neurophysiological theories that MI-EEG signals exhibit distinct frequency responses and spatial topologies across different time windows[10,11]. Consequently, the features extracted by the spatial and spectral filters across multiple time windows complement each other, enhancing overall separability and improving classification accuracy for CTSSP.

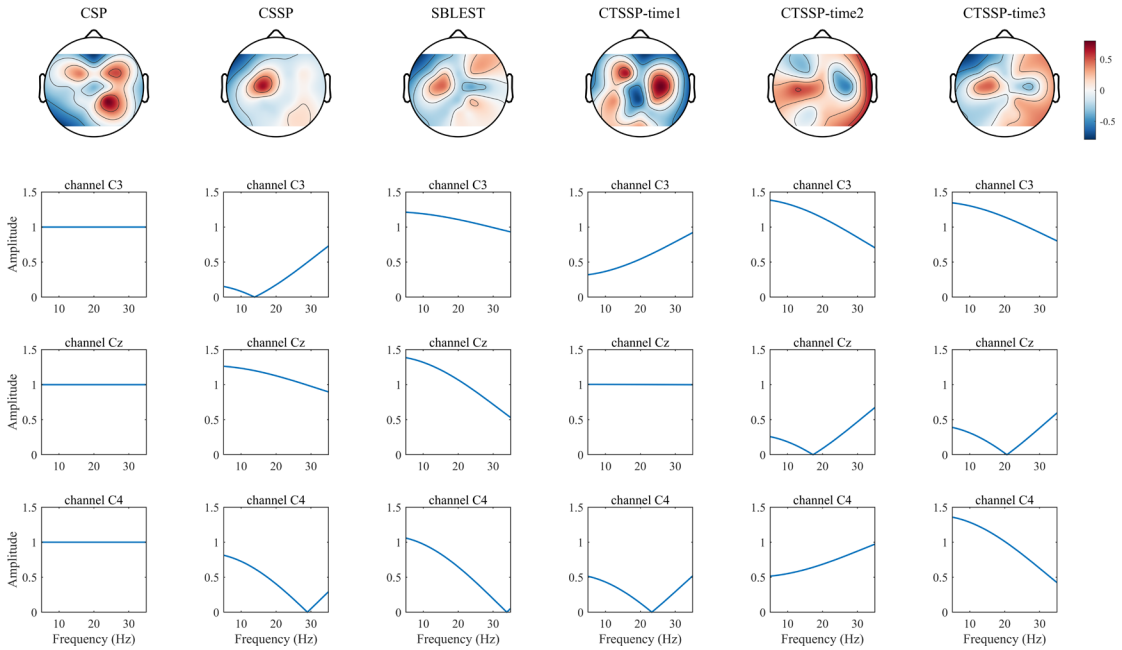

Fig. 2. Scalp topographies of the optimized spatial filters and the corresponding amplitude-frequency response curves of the three primary channels (C3, Cz, and C4) for subject S5 from dataset I. The weight maps of CSP, CSSP, and SBLEST are associated with the most discriminative eigenvalues, while the weight maps of CTSSP are linked to the most discriminative eigenvalues of three time windows.

4.2 Within-subject Classification Results

Fig. 3 compares the within-subject classification accuracies of CTSSP with those of all competing algorithms across the 143 subjects. Points above the diagonal line indicate that CTSSP outperforms the other algorithms. The results show that CTSSP improves the within-subject classification accuracy of most subjects compared to the competing algorithms. **Table 3** presents the average within-subject classification accuracy (mean ± standard deviation) of all algorithms across the five public datasets, with the best-performing algorithm for each dataset highlighted in bold. Detailed within-subject classification accuracy results for all subjects are provided in **Table B1** in **Appendix B**. The findings show that CTSSP achieved the highest average classification accuracy across all datasets. On average, CTSSP reached 76.9%, outperforming CSP, CSSP, FBCSP, SBLEST, sCNN, dCNN, EEGNet, LMDA-Net, and CSPNet by 5.8%, 4.5%, 5.9%, 2.6%, 6.3%, 14.6%, 12.0%, 13.0%, and 4.3%, respectively. Furthermore, **Fig. 4** presents the statistical differences in the average within-subject classification accuracies between the competing algorithms. The results indicate that CTSSP significantly outperforms all other algorithms (all p-values < 0.001).

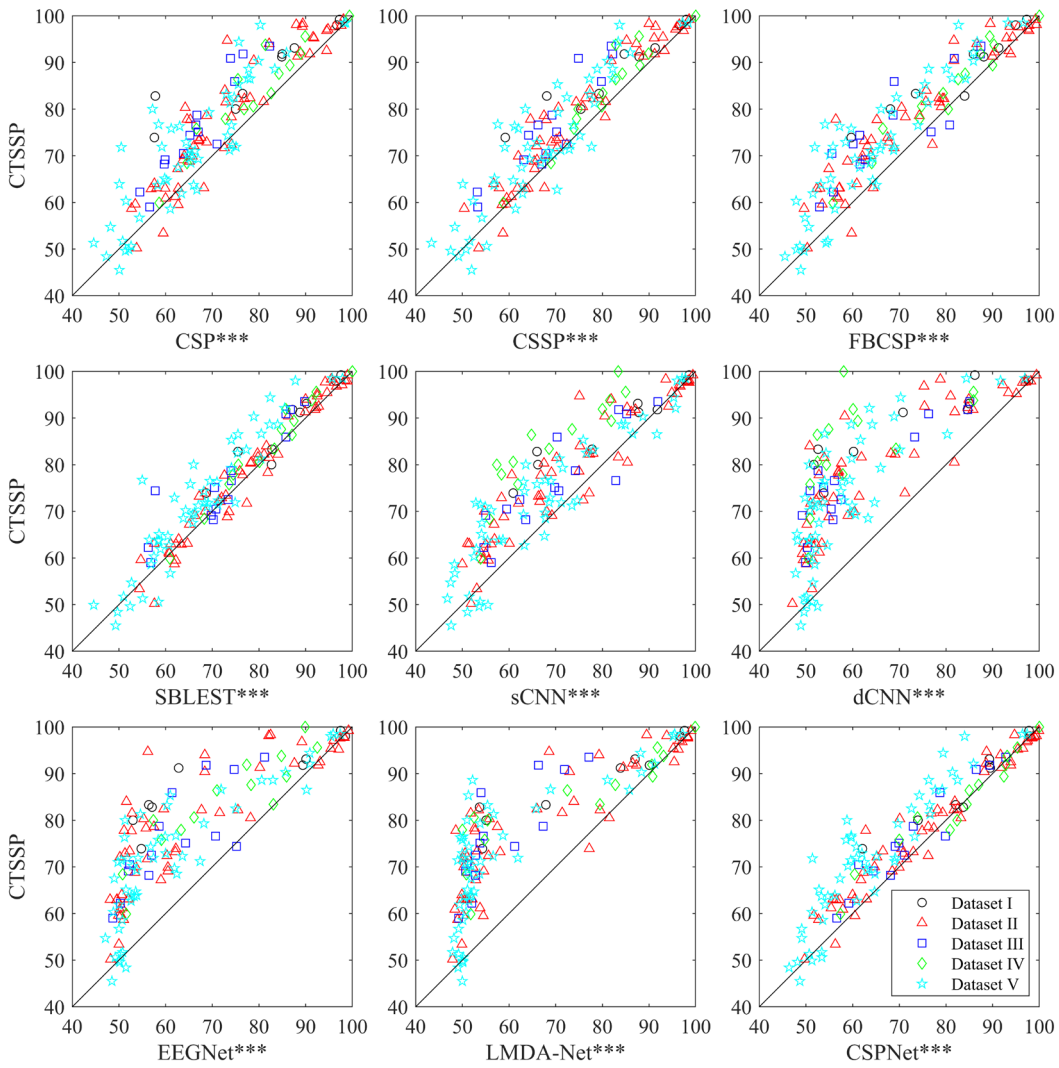

Fig. 3. Within-subject classification accuracies (%) of the competing algorithms compared to CTSSP on the 143 subjects. *** $p < 0.001$.

Table 3. Average within-subject classification accuracy (%) of CSP, CSSP, FBCSP, SBLEST, sCNN, dCNN, EEGNet, LMDA-Net, CSPNet, and CTSSP across different datasets. The highest average accuracy for each dataset is highlighted in bold.

Algorithms	Dataset I	Dataset II	Dataset III	Dataset IV	Dataset V	All
CSP	79.8±14.6	73.5±13.2	67.0±8.0	79.1±11.0	66.0±12.3	71.1±13.1
CSSP	82.3±13.0	74.8±13.5	69.0±9.1	80.5±10.1	67.0±12.5	72.4±13.3
FBCSP	82.5±12.8	73.4±15.5	68.7±12.0	79.9±11.9	64.6±13.0	71.0±14.8
SBLEST	85.5±9.4	77.5±13.5	73.0±11.1	81.8±10.4	67.4±11.9	74.3±13.4
sCNN	81.6±14.4	72.8±16.0	70.0±12.2	69.1±11.5	66.9±15.0	70.6±15.1
dCNN	71.4±17.5	65.7±16.9	60.8±13.1	60.3±12.0	58.1±10.8	62.3±14.5
EEGNet	73.3±19.9	65.7±17.4	62.2±10.4	72.2±14.3	61.3±14.7	64.9±16.0
LMDA-Net	76.3±18.5	66.6±18.7	58.2±8.9	72.6±19.2	58.2±14.5	63.9±17.4
CSPNet	85.1±11.4	75.9±15.4	72.9±11.3	82.5±12.9	64.2±12.6	72.6±15.1
CTSSP	**88.1±8.6**	**78.2±13.9**	**76.3±10.8**	**83.6±10.9**	**71.8±14.0**	**76.9±13.8**

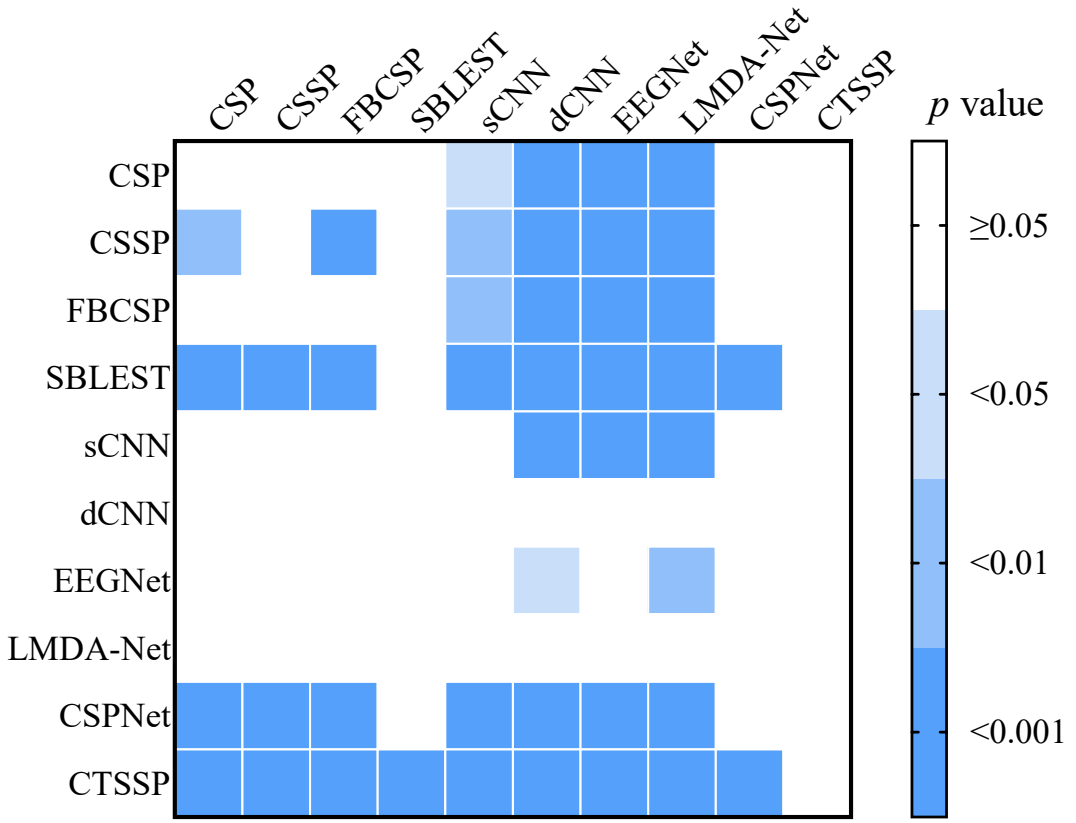

Fig. 4. Statistical analyses of within-subject classification results for different methods. The filled square indicates that the method in the row outperforms the method in the column.

4.3 Cross-session Classification Results

Fig. 5 compares the cross-session classification accuracies of CTSSP with those of all competing algorithms across 77 subjects. Points above the diagonal line indicate the superiority of CTSSP. The results show that CTSSP improves cross-session classification accuracy for most subjects compared to the competing algorithms. **Table 4** presents the average cross-session classification accuracy (mean ± standard deviation) for all algorithms across the first three publicly available datasets, with the best-performing algorithm for each dataset highlighted in bold. Detailed cross-session classification accuracy results for all subjects are provided in **Table B2** in **Appendix B**. The findings show that CTSSP achieved the highest average classification accuracy across all datasets. On average, CTSSP reached 68.8%, outperforming CSP, CSSP, FBCSP, SBLEST, sCNN, dCNN, EEGNet, LMDA-Net, and CSPNet by 4.3%, 3.7%, 2.4%, 2.5%, 7.4%, 13.8%, 10.9%, 10.2%, and 4.4%, respectively. Furthermore, **Fig. 6** shows the statistical differences in average cross-session classification accuracies between the competing algorithms. The results indicate that CTSSP significantly outperforms all other algorithms (all p-values < 0.05).

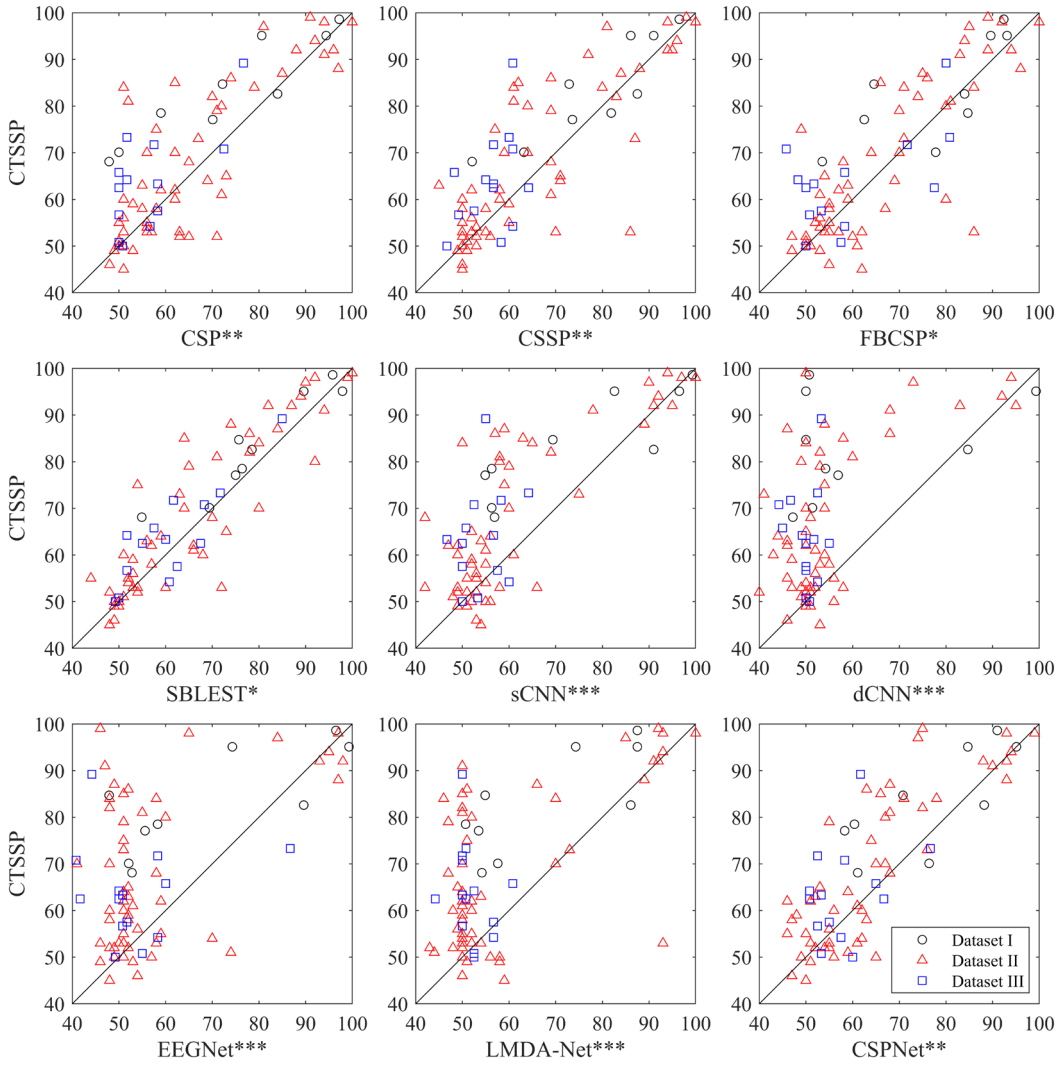

Fig. 5. Cross-session classification accuracies (%) of the competing algorithms compared to CTSSP on the 77 subjects. *** $p < 0.001$, ** $p < 0.01$, * $p < 0.05$.

Table 4. Average cross-session classification accuracy (%) of CSP, CSSP, FBCSP, SBLEST, sCNN, dCNN, EEGNet, LMDA-Net, CSPNet, and CTSSP across different datasets. The highest average accuracy for each dataset is highlighted in bold.

Algorithms	Dataset I	Dataset II	Dataset III	All
CSP	72.8±18.0	65.3±15.0	56.0±8.6	64.5±15.0
CSSP	78.3±14.2	65.2±15.9	56.2±5.3	65.1±15.4
FBCSP	78.0±14.5	66.3±14.8	59.6±12.5	66.5±15.0
SBLEST	79.2±13.5	65.5±15.6	60.9±9.9	66.3±15.2
sCNN	73.7±18.8	61.2±15.2	53.9±4.9	61.4±15.2
dCNN	60.5±18.4	55.3±13.2	50.1±3.1	55.0±12.9
EEGNet	69.6±20.7	57.1±14.4	53.4±11.2	57.9±15.2
LMDA-Net	67.4±16.2	58.9±16.1	52.0±4.0	58.6±15.1
CSPNet	76.2±14.2	64.1±14.3	58.2±7.4	64.4±14.1
CTSSP	**83.3±11.1**	**67.7±16.7**	**63.8±10.4**	**68.8±16.0**

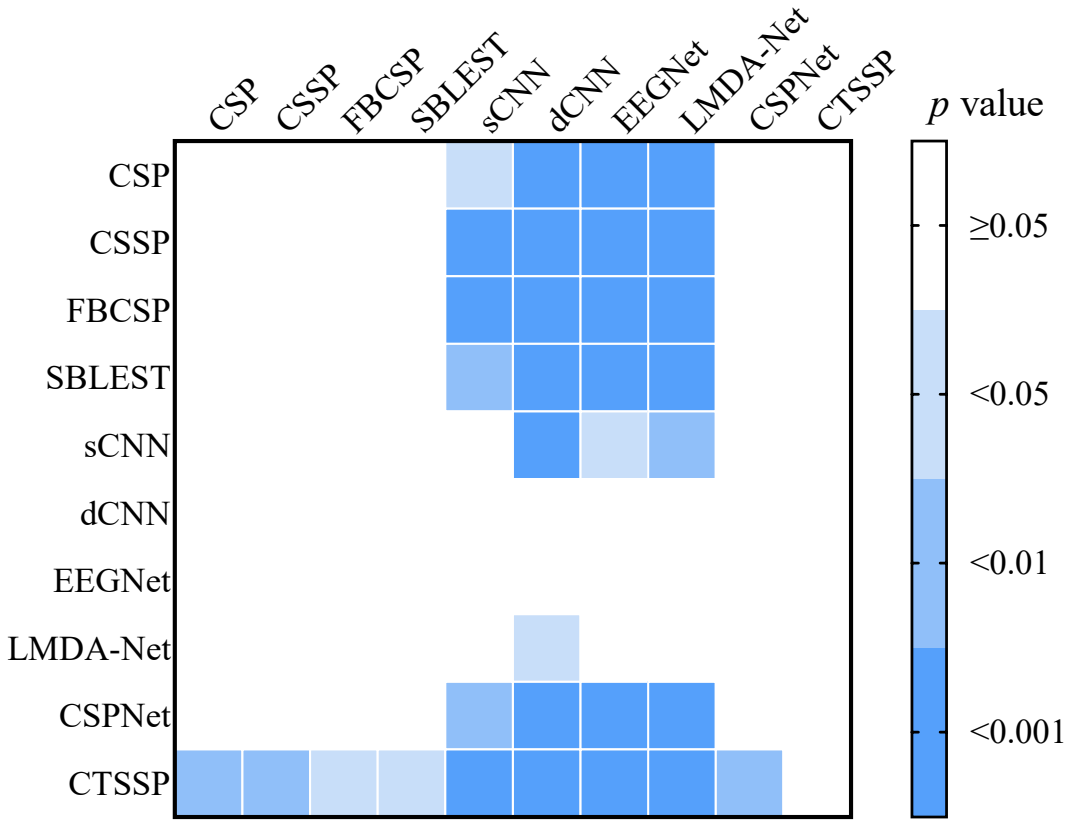

Fig. 6. Statistical analyses of cross-session classification results for different methods. The filled square indicates that the method in the row outperforms the method in the column.

4.4 Impact of Time Window Parameters on CTSSP Performance

Table 5 presents the cross-session classification performance of CTSSP with different time window configurations, with the highest average accuracy for each dataset highlighted in bold. The results show that when the time window configuration $N_t = 3$ (0–3s, 0.5–3.5s, 1–4s) is used, CTSSP achieves the highest average classification accuracy (68.8%), outperforming other configurations by 0.2% to 1.5%. The two $N_t = 2$ configurations (0–2s, 2–4s and 0–3s, 1–4s) yielded the lowest performance, with an average accuracy of 67.3%. The $N_t = 4$ configuration (0–2.5s, 0.5–3s, 1–3.5s, 1.5–4s) achieved an accuracy of 68.6%, close to the optimal performance, suggesting that increasing the number of time windows may slightly improve feature discriminability. Statistical comparisons show that, except for the $N_t = 2$ configuration (0–3s, 1–4s) ($p < 0.05$), there were no significant differences between the best configuration and other settings ($p > 0.05$). This suggests that while a higher number of time windows may improve performance by covering more dynamic neural stages, CTSSP exhibits strong robustness across different time window designs.

Table 5. Cross-session classification accuracy (%) of CTSSP with different time window configurations. The highest average accuracy for each dataset is highlighted in bold.

Time windows	Dataset I	Dataset II	Dataset III	All	p-value
$N_t = 2$: 0-2s, 2-4s	79.5±13.0	67.0±15.3	60.7±9.3	67.3±14.9	>0.05
$N_t = 2$: 0-3s, 1-4s	80.9±11.4	66.3±15.9	62.3±9.1	67.3±15.2	<0.05
$N_t = 3$: 0-2s, 1-3s, 2-4s	81.7±11.1	67.5±15.6	59.9±10.0	67.8±15.3	>0.05
$N_t = 3$: 0-3s, 0.5-3.5s, 1-4s	**83.3±11.1**	67.7±16.7	**63.8±10.4**	**68.8±16.0**	—
$N_t = 4$: 0-2.5s, 0.5-3s, 1-3.5s, 1.5-4s	82.8±11.2	**68.5±16.7**	59.8±10.9	68.6±16.3	>0.05

4.5 Impact of Time Delay Parameters on CTSSP Performance

Table 6 presents the cross-session classification performance of CTSSP under different time window configurations, with the highest average accuracy for each dataset highlighted in bold. The results show that all configurations achieve statistically indistinguishable performance, as no significant differences are observed between any pairs ($p > 0.05$). For example, the configuration with $N_d = 3$ yields the highest mean accuracy of 69.1%, marginally surpassing other configurations by 0.2% to 0.8%. Even configurations with longer delays (e.g., $d \in \{0,5\}$) maintain robust performance (68.3%), indicating that CTSSP is minimally sensitive to delay parameter selection within the tested range. This consistency highlights CTSSP's inherent robustness to variations in temporal delay. While increasing the number of delay points may slightly improve temporal feature representation (e.g., 69.1% for $N_d = 3$ vs. 68.9% for $N_d = 2$), the differences are negligible in practice.

Table 6. Cross-session classification accuracy (%) of CTSSP with different delay point configurations. The highest average accuracy for each dataset is highlighted in bold.

Delay points	Dataset I	Dataset II	Dataset III	All	p-value
$N_d = 2$: $d \in \{0,1\}$	83.3±11.1	67.7±16.7	63.8±10.4	68.8±16.0	—
$N_d = 2$: $d \in \{0,2\}$	82.6±12.4	67.8±16.7	64.0±11.0	68.8±16.1	>0.05
$N_d = 2$: $d \in \{0,3\}$	83.5±11.1	67.9±16.7	63.8±11.9	68.9±16.2	>0.05
$N_d = 2$: $d \in \{0,4\}$	83.0±10.9	67.3±16.9	**64.5±13.0**	68.6±16.4	>0.05
$N_d = 2$: $d \in \{0,5\}$	80.2±13.2	67.5±16.6	64.0±13.3	68.3±16.2	>0.05
$N_d = 3$: $d \in \{0,1,2\}$	**85.7±11.2**	68.8±17.5	59.5±9.8	69.1±17.1	>0.05
$N_d = 3$: $d \in \{0,1,3\}$	**85.7±10.9**	**68.9±17.5**	59.5±10.3	**69.1±17.1**	>0.05
$N_d = 3$: $d \in \{0,2,3\}$	85.6±10.9	68.8±17.5	59.6±10.2	69.1±17.1	>0.05

5. Discussion

5.1 Connections with Existing Methods

The proposed CTSSP framework generalizes several existing spectral-spatial filtering methods by introducing temporal adaptability and joint optimization. Classic

algorithms such as CSP, CSSP, and SBLEST can be considered special cases of CTSSP under specific parameter settings. For example:

1) When $N_t = 1$, $N_d = 0$, and $\rho = 0$, CTSSP simplifies to CSP[12], ignoring temporal dynamics and spectral adjustments;
2) When $N_t = 1$ and $\rho = 0$, CTSSP simplifies to CSSP[18], ignoring temporal dynamics;
3) When $N_t = 1$, CTSSP aligns with SBLEST[35], but lacks multi-window temporal discrimination;
4) When $N_t = 1$, $N_d = 0$, and the regularization term is modified to the L2 norm of **W**, CTSSP becomes TRCSP[19];
5) When $N_t = 1$ and the regularization term is modified to the L2 norm of **W**, STRCSP[43] is obtained.

This hierarchical relationship underscores the flexibility of CTSSP in unified temporal, spectral, and spatial feature extraction. Unlike deep learning methods (such as EEGNet, LMDA-Net, and CSPNet), which rely on black-box architectures, CTSSP offers interpretable temporal-spectral-spatial filters that align with neurophysiological principles. Specifically, the spatial localization weights in the motor cortex and the time-varying frequency responses (as shown in **Fig. 2**) reflect the known neural correlates of MI tasks[10,11]. This interpretability is crucial for clinical applications, as identifying biomarkers in clinical settings is essential for disease diagnosis and treatment.

5.2 Robustness to Temporal and Spectral Parameterization

CTSSP's robustness to variations in time window design and delay point selection underscores its adaptability to the non-stationary nature of MI-EEG signals.

As shown in **Table 5**, the configuration $N_t = 3$ (0–3s, 0.5–3.5s, 1–4s) achieved the highest cross-session classification accuracy (68.8%), potentially capturing transitional stages of MI-related neural dynamics, such as the initial ERD and subsequent beta rebound[10,11]. The use of overlapping windows helps mitigate spectral leakage and capture gradual transitions in spectral-spatial patterns, which aligns with the non-stationary nature of EEG signals. Despite small numerical differences in accuracy (ranging from 67.3% to 68.8%), no significant statistical differences were observed between the best $N_t = 3$ configuration and most alternative configurations ($p > 0.05$), demonstrating CTSSP's robustness to time window design. This characteristic is especially advantageous in practical applications, where optimizing parameters can be challenging.

Time delay parameters govern the FIR filter design and directly influence spectral feature extraction. As shown in **Table 6**, while configurations with $N_d = 3$ delays achieved marginally higher accuracy (69.1%), the lack of statistical significance ($p > 0.05$) across all delay settings suggests that CTSSP's FIR filters are robust to temporal shifts in spectral components. This robustness may arise from the algorithm's joint optimization of spatial and spectral projections, which compensates for minor variations in delay-induced phase shifts.

CTSSP's insensitivity to temporal-spectral parameterization simplifies its deployment in clinical and ambulatory settings, making it a versatile tool for real-world applications. However, the performance of the algorithm may degrade when extreme parameter choices are made, such as overly sparse windows or excessive delays, as observed in the $N_t = 2$ (0–2s, 2–4s) and $N_d = 2$: $d \in \{0,5\}$ configurations.

5.3 Performance Superiority and Neural Basis

CTSSP outperformed all competing methods in both within-subject and cross-session classification tasks (**Table 3** and **4**, **Fig. 3** to **Fig. 6**). The potential reasons for this advantage include:

1) Multi-time-window dynamic modeling: By dividing the MI task into multiple time windows, CTSSP extracts complementary features that reflect different neurophysiological stages (e.g., initial motor planning and sustained imagery[44]).
2) Spectral-spatial synergy enhancement: As shown in **Fig. 2**, CTSSP flexibly constructs spatial filters and FIR filters for the signals of each time window and channel, adaptively suppressing noise while amplifying task-relevant signal features.
3) Regularization-driven generalization: Low-rank constraints reduce model complexity by limiting the number of filters, enhancing robustness to time window parameters and improving generalization in cross-session scenarios.

The improvements in CTSSP are statistically significant (within-subject: $p < 0.001$, cross-session: $p < 0.05$), emphasizing its robustness across different datasets. Notably, SBLEST did not show significant improvement in cross-session tasks over traditional machine learning methods like CSP, CSSP, and FBCSP, further supporting the advantages of multi-time-window dynamic modeling. Additionally, compared to deep learning methods, CTSSP's improvement (e.g., 12.0% and 10.9% better than EEGNet in within-subject and cross-session classification, respectively) highlights the advantage of model-driven approaches in the context of limited training data, a common challenge in EEG-based BCIs.

5.4 Limitations and Future Work

While CTSSP represents a significant advancement in MI-EEG decoding, several limitations should be considered:

1) Computational scalability: The $\mathcal{O}(N_t^2 N_d^2 N_c^2)$ complexity of covariance matrix computations may limit real-time deployment in MI-BCIs with constrained computational resources. Future work could explore tensor decomposition[45] or online incremental learning[46] methods to reduce computational overhead.
2) Cross-domain generalization: Although CTSSP demonstrates excellent cross-session performance, its effectiveness on heterogeneous datasets (such as subject-to-subject variability) remains to be tested. Adversarial domain adaptation[47] could enhance its applicability.
3) Dynamic parameter tuning: While CTSSP is robust to fixed time window and delay point configurations, adaptive optimization of time window parameters N_t

and FIR filter order N_d during training (e.g., through meta-learning[48]) could provide additional performance gains.

In addition to MI decoding, the CTSSP framework can be extended to other EEG paradigms that require temporal-spectral-spatial discrimination, such as motor execution[49], P300[50], SSVEP[51]. Its interpretable filters also aid in discovering biomarkers for neurodegenerative diseases, such as Parkinson's disease[52]. Furthermore, integrating CTSSP with edge computing architectures could enable real-time BCIs for assistive technologies, bridging the gap between algorithm innovation and clinical translation.

6. Conclusion

This paper introduces a novel CTSSP algorithm, which combines multi-time window segmentation, adaptive spectral filtering, and low-rank spatial projection for co-optimization. CTSSP effectively captures the dynamic neural responses of MI EEG while mitigating the interference caused by cross-session variability. The visualization of the filters demonstrates CTSSP's alignment with the neural mechanisms of the motor cortex, providing interpretability for decoding the time-spectral-spatial features of MI tasks. Experimental results show that CTSSP significantly improves classification accuracy in both within-subject and cross-session scenarios, exhibiting strong robustness with respect to time-window and delay point parameter settings.

Although CTSSP represents a notable advancement in classification accuracy, its computational complexity remains a limitation for real-time applications. Future work could focus on the following directions to further enhance CTSSP's performance: (1) optimizing covariance matrix computation through tensor decomposition or incremental learning methods to reduce computational overhead; (2) developing dynamic time-window and adaptive filter order selection strategies to improve the analysis of non-stationary signals; (3) validating the generalizability of CTSSP in cross-modal (e.g., EEG-fNIRS fusion) and cross-paradigm (e.g., P300, SSVEP) tasks. These improvements are expected to accelerate the practical implementation of CTSSP in fields such as neuro-rehabilitation and wearable BCI, while offering a new methodological framework for temporal-spectral-spatial joint modeling.

Declaration of competing interest

The authors declare that they have no known competing financial interests or personal relationships that could have appeared to influence the work reported in this paper.

Data availability

The data are already publicly available. The code for this research is available at https://github.com/PLC-TJU/CTSSP.

Acknowledgements

This work was supported by STI 2030—Major Projects (No. 2022ZD0208900), and National Natural Science Foundation of China (No. 82330064，81925020，62206198，62006014).

References

[1] J.R. Wolpaw, J.D.R. Millan, N.F. Ramsey, Brain-computer interfaces: Definitions and principles, Handb Clin Neurol 168 (2020) 15–23. https://doi.org/10.1016/B978-0-444-63934-9.00002-0.

[2] L.F. Nicolas-Alonso, J. Gomez-Gil, Brain Computer Interfaces, a Review, Sensors (Basel) 12 (2012) 1211–1279. https://doi.org/10.3390/s120201211.

[3] J.J. Daly, J.R. Wolpaw, Brain–computer interfaces in neurological rehabilitation, The Lancet Neurology 7 (2008) 1032–1043. https://doi.org/10.1016/S1474-4422(08)70223-0.

[4] R. Sitaram, T. Ros, L. Stoeckel, S. Haller, F. Scharnowski, J. Lewis-Peacock, N. Weiskopf, M.L. Blefari, M. Rana, E. Oblak, N. Birbaumer, J. Sulzer, Closed-loop brain training: the science of neurofeedback, Nat Rev Neurosci 18 (2017) 86–100. https://doi.org/10.1038/nrn.2016.164.

[5] K.K. Ang, C. Guan, K.S. Phua, C. Wang, L. Zhou, K.Y. Tang, G.J. Ephraim Joseph, C.W.K. Kuah, K.S.G. Chua, Brain-computer interface-based robotic end effector system for wrist and hand rehabilitation: results of a three-armed randomized controlled trial for chronic stroke, Front. Neuroeng. 7 (2014). https://doi.org/10.3389/fneng.2014.00030.

[6] A. Ramos-Murguialday, D. Broetz, M. Rea, L. Läer, Ö. Yilmaz, F.L. Brasil, G. Liberati, M.R. Curado, E. Garcia-Cossio, A. Vyziotis, W. Cho, M. Agostini, E. Soares, S. Soekadar, A. Caria, L.G. Cohen, N. Birbaumer, Brain-Machine-Interface in Chronic Stroke Rehabilitation: A Controlled Study, Ann Neurol 74 (2013) 100–108. https://doi.org/10.1002/ana.23879.

[7] A. Biasiucci, R. Leeb, I. Iturrate, S. Perdikis, A. Al-Khodairy, T. Corbet, A. Schnider, T. Schmidlin, H. Zhang, M. Bassolino, D. Viceic, P. Vuadens, A.G. Guggisberg, J.D.R. Millan, Brain-actuated functional electrical stimulation elicits lasting arm motor recovery after stroke, Nat Commun 9 (2018) 2421. https://doi.org/10.1038/s41467-018-04673-z.

[8] F. Lotte, L. Bougrain, A. Cichocki, M. Clerc, M. Congedo, A. Rakotomamonjy, F. Yger, A review of classification algorithms for EEG-based brain-computer interfaces: a 10 year update, J Neural Eng 15 (2018) 031005. https://doi.org/10.1088/1741-2552/aab2f2.

[9] M.K. Jaiswal, Toward a High-Resolution Neuroimaging Biomarker for Mild Traumatic Brain Injury: From Bench to Bedside, Front Neurol 6 (2015) 148. https://doi.org/10.3389/fneur.2015.00148.

[10] G. Pfurtscheller, F.H. Lopes da Silva, Event-related EEG/MEG synchronization and desynchronization: basic principles, Clinical Neurophysiology 110 (1999) 1842–1857. https://doi.org/10.1016/S1388-2457(99)00141-8.

[11] C. Neuper, G. Pfurtscheller, Event-related dynamics of cortical rhythms: frequency-specific features and functional correlates, International Journal of

Psychophysiology 43 (2001) 41–58. https://doi.org/10.1016/S0167-8760(01)00178-7.
[12] B. Blankertz, R. Tomioka, S. Lemm, M. Kawanabe, K.R. Muller, Optimizing spatial filters for robust EEG single-trial analysis, Ieee Signal Proc Mag 25 (2008) 41–56. https://doi.org/10.1109/Msp.2008.4408441.
[13] L. Pan, K. Wang, L. Xu, X. Sun, W. Yi, M. Xu, D. Ming, Riemannian geometric and ensemble learning for decoding cross-session motor imagery electroencephalography signals, J Neural Eng 20 (2023) 066011. https://doi.org/10.1088/1741-2552/ad0a01.
[14] M. Congedo, A. Barachant, R. Bhatia, Riemannian geometry for EEG-based brain-computer interfaces; a primer and a review, Brain-Computer Interfaces 4 (2017) 155–174. https://doi.org/10.1080/2326263x.2017.1297192.
[15] M. Fatourechi, A. Bashashati, R.K. Ward, G.E. Birch, EMG and EOG artifacts in brain computer interface systems: A survey, Clinical Neurophysiology 118 (2007) 480–494. https://doi.org/10.1016/j.clinph.2006.10.019.
[16] V. Jayaram, M. Alamgir, Y. Altun, B. Scholkopf, M. Grosse-Wentrup, Transfer Learning in Brain-Computer Interfaces, IEEE Computational Intelligence Magazine 11 (2016) 20–31. https://doi.org/10.1109/MCI.2015.2501545.
[17] D.R. Wu, X. Jiang, R. Peng, Transfer learning for motor imagery based brain-computer interfaces: A tutorial, Neural Netw 153 (2022) 235–253. https://doi.org/10.1016/j.neunet.2022.06.008.
[18] S. Lemm, B. Blankertz, G. Curio, K.R. Muller, Spatio-spectral filters for improving the classification of single trial EEG, IEEE Trans Biomed Eng 52 (2005) 1541–8. https://doi.org/10.1109/TBME.2005.851521.
[19] F. Lotte, C. Guan, Regularizing common spatial patterns to improve BCI designs: unified theory and new algorithms, IEEE Trans Biomed Eng 58 (2011) 355–62. https://doi.org/10.1109/TBME.2010.2082539.
[20] A. Barachant, S. Bonnet, M. Congedo, C. Jutten, Multiclass brain-computer interface classification by Riemannian geometry, IEEE Trans Biomed Eng 59 (2012) 920–8. https://doi.org/10.1109/TBME.2011.2172210.
[21] L. Pan, K. Wang, X. Sun, M. Xu, D. Ming, Riemannian Geometry-Based Spatial Filtering (RSF) Method for Motor Imagery EEG Classification, in: Proceedings of the 2024 9th International Conference on Biomedical Signal and Image Processing, ACM, Suzhou China, 2024: pp. 48–54. https://doi.org/10.1145/3691521.3691529.
[22] L. Pan, K. Wang, Y. Huang, X. Sun, J. Meng, W. Yi, M. Xu, T.-P. Jung, D. Ming, Enhancing motor imagery EEG classification with a Riemannian geometry-based spatial filtering (RSF) method, Neural Networks 188 (2025) 107511. https://doi.org/10.1016/j.neunet.2025.107511.
[23] L. Pan, X. Sun, K. Wang, Y. Cao, M. Xu, D. Ming, Cross-session motor imagery-electroencephalography decoding with Riemannian spatial filtering and domain adaptation, Journal of Biomedical Engineering 42 (2025) 272–279. https://doi.org/10.7507/1001-5515.202411035.

[24] K.K. Ang, Z.Y. Chin, C. Wang, C. Guan, H. Zhang, Filter Bank Common Spatial Pattern Algorithm on BCI Competition IV Datasets 2a and 2b, Front Neurosci 6 (2012) 39. https://doi.org/10.3389/fnins.2012.00039.
[25] Y. Zhang, C.S. Nam, G. Zhou, J. Jin, X. Wang, A. Cichocki, Temporally Constrained Sparse Group Spatial Patterns for Motor Imagery BCI, IEEE Trans Cybern 49 (2019) 3322–3332. https://doi.org/10.1109/TCYB.2018.2841847.
[26] O.Y. Kwon, M.-H. Lee, C. Guan, S.-W. Lee, Subject-Independent Brain-Computer Interfaces Based on Deep Convolutional Neural Networks, IEEE Transactions on Neural Networks and Learning Systems 31 (2020) 3839–3852. https://doi.org/10.1109/tnnls.2019.2946869.
[27] Ravikiran Mane, Effie Chew, Karen Chua, Kai Keng Ang, Neethu Robinson, A. P. Vinod, Seong-Whan Lee, Cuntai Guan, FBCNet: A multi-view convolutional neural network for brain-computer interface, arXiv Preprint 2104.01233 (2021).
[28] H. Altaheri, G. Muhammad, M. Alsulaiman, Physics-Informed Attention Temporal Convolutional Network for EEG-Based Motor Imagery Classification, IEEE Trans. Ind. Inf. 19 (2023) 2249–2258. https://doi.org/10.1109/TII.2022.3197419.
[29] H. Altaheri, G. Muhammad, M. Alsulaiman, S.U. Amin, G.A. Altuwaijri, W. Abdul, M.A. Bencherif, M. Faisal, Deep learning techniques for classification of electroencephalogram (EEG) motor imagery (MI) signals: a review, Neural Comput & Applic 35 (2023) 14681–14722. https://doi.org/10.1007/s00521-021-06352-5.
[30] R.T. Schirrmeister, J.T. Springenberg, L.D.J. Fiederer, M. Glasstetter, K. Eggensperger, M. Tangermann, F. Hutter, W. Burgard, T. Ball, Deep learning with convolutional neural networks for EEG decoding and visualization, Hum Brain Mapp 38 (2017) 5391–5420. https://doi.org/10.1002/hbm.23730.
[31] V.J. Lawhern, A.J. Solon, N.R. Waytowich, S.M. Gordon, C.P. Hung, B.J. Lance, EEGNet: a compact convolutional neural network for EEG-based brain-computer interfaces, J Neural Eng 15 (2018) 056013. https://doi.org/10.1088/1741-2552/aace8c.
[32] Z. Miao, M. Zhao, X. Zhang, D. Ming, LMDA-Net:A lightweight multi-dimensional attention network for general EEG-based brain-computer interfaces and interpretability, Neuroimage 276 (2023) 120209. https://doi.org/10.1016/j.neuroimage.2023.120209.
[33] C. Ju, C. Guan, Graph Neural Networks on SPD Manifolds for Motor Imagery Classification: A Perspective From the Time-Frequency Analysis, IEEE Trans Neural Netw Learn Syst PP (2023) 1–15. https://doi.org/10.1109/TNNLS.2023.3307470.
[34] C. Ju, C. Guan, Tensor-CSPNet: A Novel Geometric Deep Learning Framework for Motor Imagery Classification, IEEE Trans Neural Netw Learn Syst 34 (2023) 10955–10969. https://doi.org/10.1109/TNNLS.2022.3172108.
[35] W. Wang, F. Qi, D.P. Wipf, C. Cai, T. Yu, Y. Li, Y. Zhang, Z. Yu, W. Wu, Sparse Bayesian Learning for End-to-End EEG Decoding, IEEE Transactions on Pattern

Analysis and Machine Intelligence 45 (2023) 15632–15649. https://doi.org/10.1109/tpami.2023.3299568.
[36] F. Qi, W. Wu, Z.L. Yu, Z. Gu, Z. Wen, T. Yu, Y. Li, Spatiotemporal-Filtering-Based Channel Selection for Single-Trial EEG Classification, IEEE Trans Cybern 51 (2021) 558–567. https://doi.org/10.1109/TCYB.2019.2963709.
[37] M. Tangermann, K.R. Muller, A. Aertsen, N. Birbaumer, C. Braun, C. Brunner, R. Leeb, C. Mehring, K.J. Miller, G.R. Muller-Putz, G. Nolte, G. Pfurtscheller, H. Preissl, G. Schalk, A. Schlogl, C. Vidaurre, S. Waldert, B. Blankertz, Review of the BCI Competition IV, Front Neurosci 6 (2012) 55. https://doi.org/10.3389/fnins.2012.00055.
[38] M.H. Lee, O.Y. Kwon, Y.J. Kim, H.K. Kim, Y.E. Lee, J. Williamson, S. Fazli, S.W. Lee, EEG dataset and OpenBMI toolbox for three BCI paradigms: an investigation into BCI illiteracy, Gigascience 8 (2019). https://doi.org/10.1093/gigascience/giz002.
[39] D. Steyrl, R. Scherer, J. Faller, G.R. Müller-Putz, Random forests in non-invasive sensorimotor rhythm brain-computer interfaces: a practical and convenient non-linear classifier, Biomedical Engineering / Biomedizinische Technik 61 (2016) 77–86. https://doi.org/10.1515/bmt-2014-0117.
[40] H. Cho, M. Ahn, S. Ahn, M. Kwon, S.C. Jun, EEG datasets for motor imagery brain-computer interface, Gigascience 6 (2017) 1–8. https://doi.org/10.1093/gigascience/gix034.
[41] V. Jayaram, A. Barachant, MOABB: trustworthy algorithm benchmarking for BCIs, J Neural Eng 15 (2018) 066011. https://doi.org/10.1088/1741-2552/aadea0.
[42] H. He, D. Wu, Transfer Learning for Brain-Computer Interfaces: A Euclidean Space Data Alignment Approach, IEEE Trans Biomed Eng 67 (2020) 399–410. https://doi.org/10.1109/TBME.2019.2913914.
[43] F. Qi, Y. Li, W. Wu, RSTFC: A Novel Algorithm for Spatio-Temporal Filtering and Classification of Single-Trial EEG, IEEE Transactions on Neural Networks and Learning Systems 26 (2015) 3070–3082. https://doi.org/10.1109/TNNLS.2015.2402694.
[44] K. Wang, M. Xu, Y. Wang, S. Zhang, L. Chen, D. Ming, Enhance decoding of pre-movement EEG patterns for brain-computer interfaces, J Neural Eng 17 (2020) 016033. https://doi.org/10.1088/1741-2552/ab598f.
[45] T.G. Kolda, B.W. Bader, Tensor Decompositions and Applications, SIAM Rev. 51 (2009) 455–500. https://doi.org/10.1137/07070111X.
[46] Online SSVEP-based BCI using Riemannian geometry, Neurocomputing 191 (2016) 55–68. https://doi.org/10.1016/j.neucom.2016.01.007.
[47] Y. Ganin, E. Ustinova, H. Ajakan, P. Germain, H. Larochelle, F. Laviolette, M. Marchand, V. Lempitsky, Domain-adversarial training of neural networks, J. Mach. Learn. Res. 17 (2016) 2096–2030.
[48] T. Hospedales, A. Antoniou, P. Micaelli, A. Storkey, Meta-Learning in Neural Networks: A Survey, IEEE Transactions on Pattern Analysis and Machine Intelligence 44 (2022) 5149–5169. https://doi.org/10.1109/TPAMI.2021.3079209.

[49] Z. Ma, X. Yang, J. Meng, K. Wang, M. Xu, D. Ming, Decoding Arm Movement Direction Using Ultra-High-Density EEG, IEEE Journal of Biomedical and Health Informatics (2025) 1–12. https://doi.org/10.1109/JBHI.2025.3545856.

[50] X.L. Xiao, M.P. Xu, J. Han, E.W. Yin, S. Liu, X. Zhang, T.P. Jung, D. Ming, Enhancement for P300-speller classification using multi-window discriminative canonical pattern matching, J. Neural Eng. 18 (2021). https://doi.org/ARTN 046079 10.1088/1741-2552/ac028b.

[51] M. Xu, J. Han, Y. Wang, T.-P. Jung, D. Ming, Implementing Over 100 Command Codes for a High-Speed Hybrid Brain-Computer Interface Using Concurrent P300 and SSVEP Features, IEEE Transactions on Biomedical Engineering 67 (2020) 3073–3082. https://doi.org/10.1109/TBME.2020.2975614.

[52] S. Waninger, C. Berka, M. Stevanovic Karic, S. Korszen, P.D. Mozley, C. Henchcliffe, Y. Kang, J. Hesterman, T. Mangoubi, A. Verma, Neurophysiological Biomarkers of Parkinson's Disease, J Parkinsons Dis 10 (2020) 471–480. https://doi.org/10.3233/JPD-191844.